Hybrid Reconstruction of Subsurface 3-D Objects Using FRTM and VBIM Enhanced by Monte Carlo Method

Xi Tang, Jiawen Li, Lixiao Wang, Feng Han, *Member, IEEE*, Hai Liu, *Member, IEEE*, and Qing Huo Liu, *Fellow, IEEE*

***Abstract*— A hybrid method is proposed to reconstruct the subsurface 3-D objects with electromagnetic fields. The frequency-domain reverse time migration (FRTM) is first used to determine the approximate locations and sizes of the objects. Then, based on these results, the full-wave inversion, the variational Born iteration method (VBIM) is used to reconstruct both the shapes and dielectric parameters of the objects. The Monte Carlo method (MCM) is adopted to further refine the reconstructed shapes. Numerical simulations show that the proposed hybrid method can be effectively used for the subsurface imaging and detection.**

***Index Terms*— Frequency-domain reverse time migration (FRTM), Monte Carlo method (MCM), subsurface imaging, variational Born iteration method (VBIM).**

I. Introduction

GROUND penetrating radar (GPR) has wide applications in subsurface imaging and detection such as pavement crack detection [1], buried pipe inspection [2], and landmine detection [3]. One of the commonly used methods for reconstructing the subsurface image is the reverse time migration (RTM), which has the advantage of high accuracy [4]. The traditional time-domain RTM (TRTM) is performed by the finite-difference time-domain (FDTD) method [5] or finite-element method [6], which can account for complex background velocity models. However, TRTM by FDTD requires high computational costs when there are a large number of source and receiver locations. The frequency-domain RTM (FRTM) proposed recently [7] can overcome this shortcoming when the background medium is horizontally layered since the dyadic Green's functions (DGFs) for the layered background medium are computed in advance. The forward and backward extrapolations for all the measurement shots are carried out simultaneously in the frequency domain. Unfortunately, both the TRTM and FRTM can only determine the approximate locations and geometry shapes of the subsurface objects. They are incapable of retrieving the dielectric parameters of the objects.

Full-wave inversion (FWI) can be used to retrieve all the model parameters of subsurface objects such as locations, shapes [8], and dielectric constants [9]. For example, in [10], Born approximation (BA) is used to retrieve both the shape and permittivity of a subsurface object. However, when the electromagnetic (EM) scattering is strong, e.g., the contrast of the object with respect to the background medium is high, or when the EM multiple scattering between two objects becomes large, BA results in large errors. A rigorous iterative method is required to obtain the model parameters of the subsurface object. Most popular deterministic iterative methods include contrast source inversion (CSI) [11], subspace optimization method (SOM) [12], and Born iteration method (BIM) [13]. CSI and SOM depend on initial solutions of the unknown model parameters of the objects. Variational BIM (VBIM) [14] is used in this letter to perform the FWI.

When the approximate locations of the subsurface objects are unknown, VBIM requires a large inversion domain to enclose the unknown objects. The computational cost is high for iterative FWI when the computation domain is large. In the previous works, the linear sampling method (LSM) [15] and the iterative multiscaling approach (IMSA) [16] are used to downsize the inversion domain before performing FWI. However, LSM usually requires the omnidirectional far-field scattered field pattern, and IMSA contains two nested iterative loops. In this letter, the low-cost FRTM is used to determine the approximate locations and shapes of the objects. Then, VBIM is only performed in the localized inversion domain to reconstruct the model parameters of the objects. The Monte Carlo method (MCM) is applied to the VBIM outputs in each iteration to further compress the inversion domain and refine the reconstructed shapes.

This letter is organized as follows. In Section II, we briefly introduce the procedures of FRTM, VBIM, and MCM, as well as their hybridization algorithm. In Section III, a typical subsurface detection model including two irregular objects is presented to validate the hybrid method. Finally, conclusions are drawn in Section IV.

Manuscript received July 20, 2019; revised October 8, 2019 and December 31, 2019; accepted February 8, 2020. Date of publication February 19, 2020; date of current version January 21, 2021. This work was supported by the National Key Research and Development Program of the Ministry of Science and Technology of China under Grant 2018YFC0603503 and Grant 2018YFF01013300. *(Corresponding authors: Feng Han; Qing Huo Liu.)*

Xi Tang, Jiawen Li, Lixiao Wang, and Feng Han are with the Key Laboratory of Electromagnetic Wave Science and Detection Technology, Institute of Electromagnetics and Acoustics, Xiamen University, Xiamen 361005, China (e-mail: feng.han@xmu.edu.cn).

Hai Liu is with the School of Civil Engineer, Guangzhou University, Guangzhou 510006, China (e-mail: hliu@gzhu.edu.cn).

Qing Huo Liu is with the Department of Electrical and Computer Engineering, Duke University, Durham, NC 27708 USA (e-mail: qhliu@duke.edu).

Color versions of one or more of the figures in this letter are available online at https://ieeexplore.ieee.org.

Digital Object Identifier 10.1109/LGRS.2020.2973244

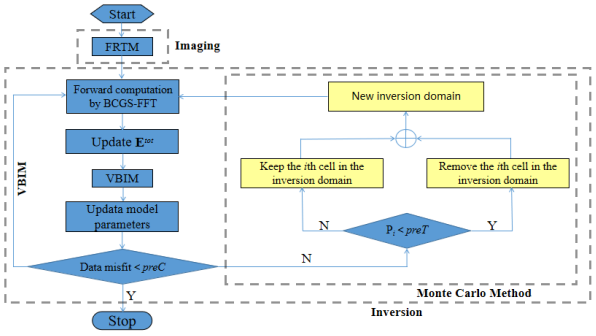

Fig. 1. Flowchart of the threefold hybridization of FRTM, VBIM, and MCM. The *preC* and *preT* are prescribed thresholds for the scattered field data misfit in VBIM and MCM, respectively.

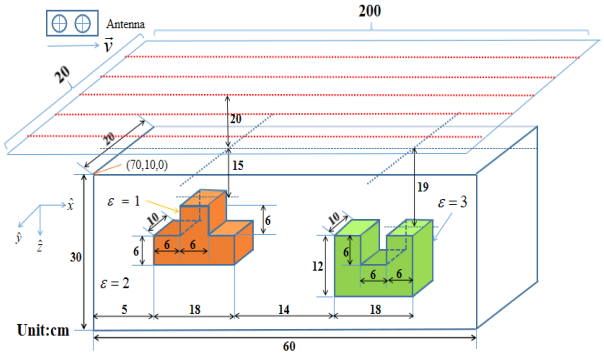

Fig. 2. 3-D GPR subsurface detection for a convex air box and a concave object. The CO antennas move 20 cm above the ground surface.

II. Methods

A. FRTM Imaging

When the background medium is horizontally layered, FRTM has the intrinsic advantage of fast imaging of subsurface objects. The detailed procedure of FRTM was presented in [7]. The main idea is to sum up all the wavefield data for all sampling frequencies. The image condition can be written as follows:

$$I(\mathbf{r}) = \frac{1}{2\pi}\int_{-\infty}^{+\infty} U_r(\mathbf{r},\omega)U_s(\mathbf{r},\omega)e^{j\omega T}\,dw \tag{1}$$

where $U_s(\mathbf{r},\omega)$ and $U_r(\mathbf{r},\omega)$ are the Fourier spectra of the source wavefield and receiver wavefield, respectively. $\mathbf{r}$ is the spatial sampling position in the imaging domain, T is the time window of the recorded GPR traces, and ω is the angular frequency. $\mathbf{U}_s(\mathbf{r},\omega)$ and $\mathbf{U}_r(\mathbf{r},\omega)$ are obtained by multiplying DGFs with the spectra of the source wavelet and receiver signals [17], respectively

$$\mathbf{U}_s(\mathbf{r},\omega) = \overline{\overline{\mathbf{G}}}(\mathbf{r},\mathbf{r}_s,\omega)\cdot\mathbf{S}(\mathbf{r}_s,\omega) \tag{2}$$

$$\mathbf{U}_r(\mathbf{r},\omega) = \overline{\overline{\mathbf{G}}}(\mathbf{r},\mathbf{r}_r,\omega)\cdot\mathbf{R}^*(\mathbf{r}_r,\omega)e^{-j\omega T} \tag{3}$$

where $\overline{\overline{\mathbf{G}}}$ is the DGF. $\mathbf{S}(\mathbf{r}_s,\omega)$ and $\mathbf{R}(\mathbf{r}_r,\omega)$ are the spectra of the source waveforms illuminated at $\mathbf{r}_s$ and the recorded signals sampled at $\mathbf{r}_r$, respectively.

B. VBIM

The VBIM is used to retrieve the dielectric parameters of the subsurface objects by solving the data equation

$$\mathbf{E}^{\text{scat}}(\mathbf{r}_r,\mathbf{r}_s) = j\omega\varepsilon_b\int_D \overline{\overline{\mathbf{G}}}_{\mathbf{EJ}}(\mathbf{r}_r,\mathbf{r}')\cdot\chi(\mathbf{r}')\mathbf{E}^{\text{tot}}(\mathbf{r}',\mathbf{r}_s)d\mathbf{r}' \tag{4}$$

where

$$\chi = \frac{\varepsilon-\varepsilon_b}{\varepsilon_b} \tag{5}$$

is the contrast of the subsurface object with respect to the background medium. The $\mathbf{E}^{\text{tot}}$ in (4) is updated by the forward solver, the stabilized biconjugate gradient fast Fourier transform (BCGS-FFT), via solving the state equation

$$\mathbf{E}^{\text{inc}}(\mathbf{r}) = \mathbf{E}^{\text{tot}}(\mathbf{r}) - j\omega\varepsilon_b\int_D \overline{\overline{\mathbf{G}}}_{\mathbf{EJ}}(\mathbf{r},\mathbf{r}')\cdot\chi(\mathbf{r}')\mathbf{E}^{\text{tot}}(\mathbf{r}',\mathbf{r}_s)d\mathbf{r}'. \tag{6}$$

When the nonlinear iterative FWI is performed, $\mathbf{E}^{\text{tot}}$ and χ are updated alternately until the mismatch between the calculated scattered field and measured scattered field reaches a stop criterion.

C. Monte Carlo Algorithm

The MCM obtains the statistical values of physical observables by sampling a large number of configurations. In this letter, we use it to gradually compress the inversion domain in VBIM. Assume the whole inversion domain is divided into I discretized cells. Because solving an inverse problem is to infer the model parameter distribution over the inversion space [18] and the data (4) partially restricts the solution of χ, the model parameter distribution in all discretized cells acquired by VBIM is pseudorandom. The ground truth is that each cell only has two states, the "background" or the "scatterer." The probability of the "scatterer" of the ith cell can be defined as follows:

$$P_i^n = \frac{\left|\varepsilon_i^n-\varepsilon_b\right|}{\max\limits_{1\leqslant i\leqslant I}\left(\left|\varepsilon_i^n-\varepsilon_b\right|\right)} \tag{7}$$

where ε_i^n is the model parameter in the ith cell given by VBIM in the nth iteration. A larger P_i^n indicates that the ith cell is more like a "scatterer" cell in the nth iteration. Therefore, we can set a threshold to classify all the discretized cells in the whole inversion domain. Those cells with smaller P_i^n will be treated as "background" cells and removed in the $(n+1)$th VBIM iteration since "background" cells have no contribution to the scattered fields at the receiver array. Therefore, the remaining cells cluster together to form the new inversion domain. As a result, the computation domain of VBIM is gradually compressed in the iterations. In this letter, the threshold is set as 15% empirically, which can guarantee that the "background" cells are effectively but stably removed. But one should keep in mind that the threshold must be reduced correspondingly for the scatterers with low contrasts or step-like inhomogeneous permittivity distribution to avoid the incorrect removal of "scatterer" cells.

D. Threefold Hybridization

When the subsurface detection is carried out, FRTM is first used to locate the approximate locations of the buried objects.

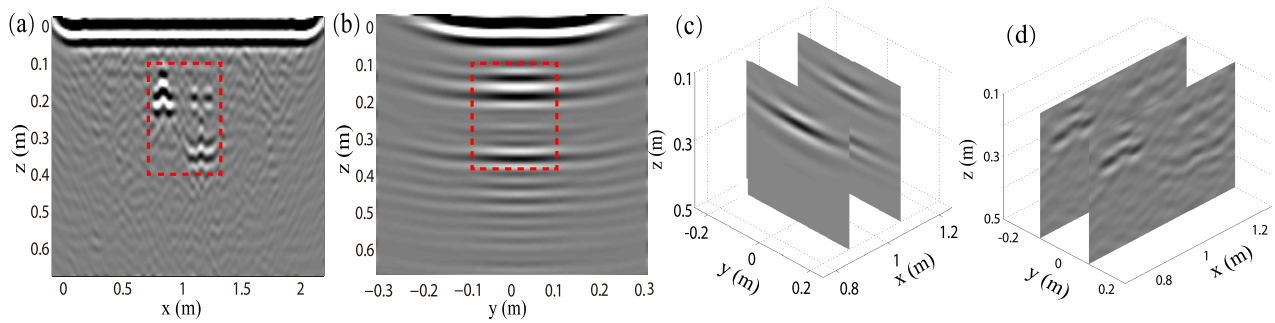

Fig. 3. FRTM imaging results. (a) 2-D front view of the imaging result at $y = 0$ m. (b) 2-D side view of the imaging result at $x = 1.1$ m. (c) Two yz slices of the imaging result at $x = 0.9$ m and $x = 1.1$ m, respectively. (d) Two xz slices of the imaging result at $y = -0.1$ m and $y = 0.1$ m, respectively. The scattered field data used for RTM are contaminated by 30 dB noise. The dotted boxes illustrate the FWI domain.

Then, we choose a localized inversion domain enclosing the objects and perform VBIM. In each iteration, MCM helps to remove the "background" cells and further reduce the inversion domain. As a result, the locations, shapes, and the dielectric parameters of the subsurface objects can be reconstructed efficiently and precisely. The flowchart of this threefold hybridization process is shown in Fig. 1.

III. Numerical Results

In this section, we design a numerical model of subsurface detection by GPR to demonstrate the accuracy and effectiveness of the proposed hybrid method. As shown in Fig. 2, two isolated objects are buried in the subsurface. The background medium has a relative dielectric constant $\epsilon_r = 2.0$ and a conductivity $\sigma = 1$ mS/m. The convex object with the relative permittivity $\epsilon_{s1} = 1.0$ is formed by adding a small cube with a size of 0.06 m $\times$ 0.10 m $\times$ 0.06 m to a rectangular shape with the dimensions of 0.18 m $\times$ 0.10 m $\times$ 0.06 m. The concave object has the relative permittivity $\epsilon_{s2} = 3.0$, which is formed by cutting a small cube with a size of 0.06 m $\times$ 0.10 m $\times$ 0.06 m out of a rectangular shape with the dimensions of 0.18 m $\times$ 0.10 m $\times$ 0.12 m. The centers of the convex object and concave object are (0.84, 0, 0.21) and (1.16, 0, 0.25) m, respectively. Two objects are 0.14 m apart. The GPR data are simulated for a pair of dipole antennas with a common offset (CO) of 10 cm and placed 20 cm above the ground. Both the transmitting and receiving antennas are linearly polarized in the $\hat{y}$-direction. The source wavelet is the Blackman–Harris window (BHW) function with a center frequency 2.0 GHz. Each 2-D CO GPR profile in the xz plane contains 201 traces with a step of 1 cm beginning at $x = 0$ cm. Totally, there are ten xz plane profiles from $y = -10$ to $+8$ cm with a step of 2 cm. All the simulations are performed by the commercial FDTD simulation software Wavenology EM. In order to simulate the real-world GPR measurements, we add 30-dB white Gaussian noise to the simulated field data. Here, the noise level is defined according to the signal-to-noise ratio (SNR) of power. Both the FRTM and VBIM with and without MCM are implemented parallelly on a workstation with 20-cores Xeon E2650 v3 2.3 G CPU, 512-GB RAM.

Fig. 3 shows the 2-D slices and 3-D profiles from FRTM results. Because the FRTM is based on layered medium DGFs, we only calculated the DGFs for the subsurface region and obtained the corresponding 3-D images. The total implementation time of FRTM is 1 h and 43 min. As shown in Fig. 3(a), two objects are clearly imaged. The positions of their top surfaces are consistent with the true positions shown in Fig. 2. Fig. 3(b) shows the yz slice of the concave object at $x = 1.1$ m. In order to display the 3-D results obtained by FRTM, we show two parallel yz slices at $x = 0.9$ m and $x = 1.1$ m in Fig. 3(c) and two parallel xz slices at $y = -0.1$ m and $y = 0.1$ m in Fig. 3(d), respectively. Because the aperture of the array of data measurement points in the x-direction is much larger than that in the y-direction, the focusing effect in the xz plane is better than that in the yz plane. We can see that FRTM only gives the approximate locations and sizes of two scatterers. The precise shapes and dielectric parameters are not available. Therefore, we choose the 3-D rectangular region with 0.7 m $\leqslant x \leqslant$ 1.3 m, -0.1 m $\leqslant y \leqslant$ 0.1 m, and 0.1 m $\leqslant z \leqslant$ 0.4 m as the computation domain to perform FWI.

In the inversion, we reconstruct the relative permittivity profiles of two objects by VBIM with and without MCM, respectively. The measured scattered field data are the same as those used for FRTM. However, in order to save the computational cost, we reduce the data sampling points used in the FWI. Right above the inversion domain, the data sampling points remain the same as those in FRTM, i.e., the spatial sampling interval is 1 cm in the x-direction and 2 cm in the y-direction. However, in two sides of the inversion domain, in the x-direction, the sampling interval is increased to 15 cm. Therefore, there are totally 610 sets of E_y data used for inversion. The inversion domain D enclosing two objects has the dimensions of 0.6 m $\times$ 0.2 m $\times$ 0.3 m and is divided into 36 000 cubic cells. Each cell has the size of $\Delta x = \Delta y = \Delta z = 0.01$ m. Hence, there are totally 36 000 unknowns. After 17 iterations, both the VBIM with and without MCM stop. The VBIM-MCM only takes 2 h and 8 min while the computation time of VBIM without MCM is around 3 h.

The 2-D xz slices of reconstructed permittivity values of the two objects by VBIM-MCM and VBIM are shown in Figs. 4 and 5, respectively. We can see that both the shapes and model parameters of the two objects are well reconstructed. VBIM-MCM obviously outperforms VBIM. We made two observations.

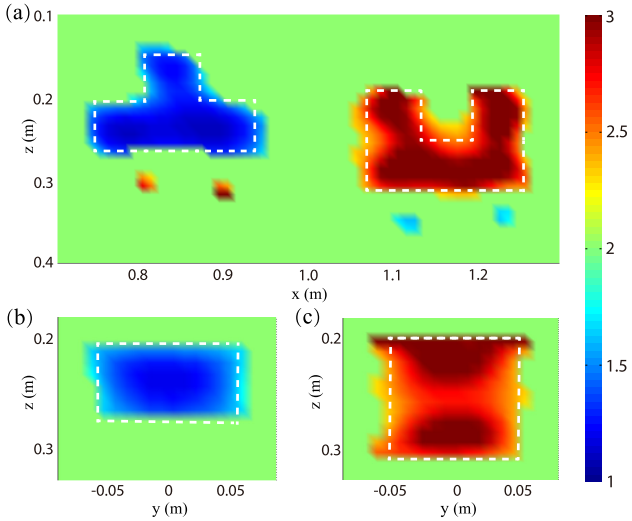

Fig. 4. FWI results by VBIM-MCM. (a) 2-D slice at $y = 0$ m. (b) 2-D slice for the convex object at $x = 0.9$ m. (c) 2-D slice for the concave object at $x = 1.1$ m. Scattered field data used for FWI are contaminated by 30 dB noise. Dotted boxes denote the true locations of the subsurface objects.

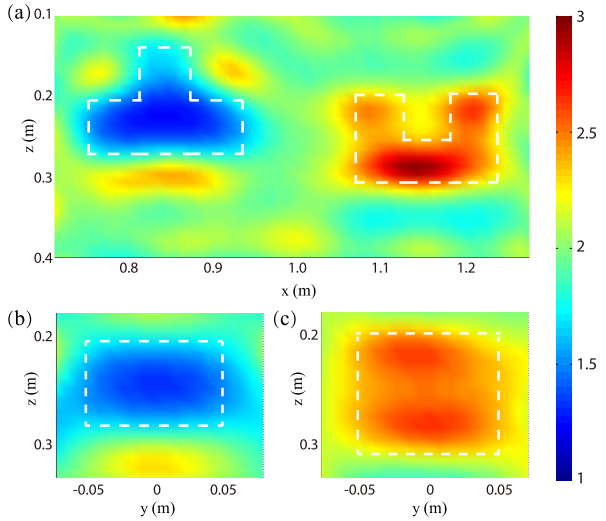

Fig. 5. FWI results by VBIM without MCM. (a) 2-D slice at $y = 0$ m. (b) 2-D slice for the convex object at $x = 0.9$ m. (c) 2-D slice for the concave object at $x = 1.1$ m. Scattered field data used for FWI are contaminated by 30 dB noise. Dotted boxes denote the true locations of the subsurface objects.

1) The shapes of the convex and concave objects are better reconstructed by VBIM-MCM compared with VBIM without MCM. The spatial distribution of the model parameters of two objects by VBIM without MCM tends to spread out. As a result, the edges and corners are blurred. On the contrary, the boundary contrasts of the two reconstructed objects with respect to the background medium are obviously shown in the results by VBIM-MCM.
2) The permittivity values of two objects reconstructed by VBIM-MCM are closer to the true values compared with those retrieved by VBIM without MCM. This is as we expect. Because the MCM further compresses the inversion domain in each VBIM iteration and, thus, reduces the number of unknowns gradually in the discretized data equation, the reconstructed model parameters become more precise since the underdetermination of the data equation is mitigated.

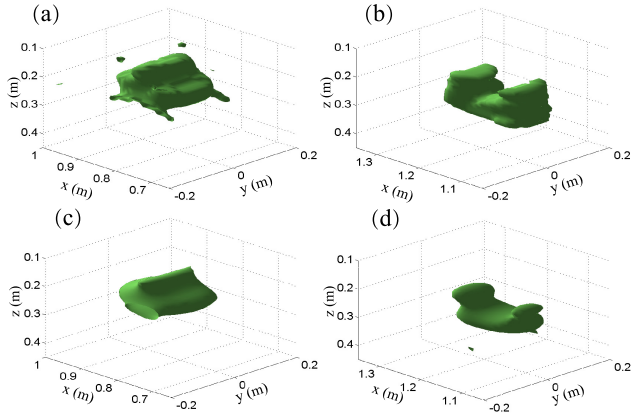

Fig. 6. 3-D iso-surfaces of relative permittivity values. (a) and (b) VBIM-MCM results. (c) and (d) VBIM results without MCM. In (a) and (c), the iso value is 1.6 and in (b) and (d), the iso value is 2.4.

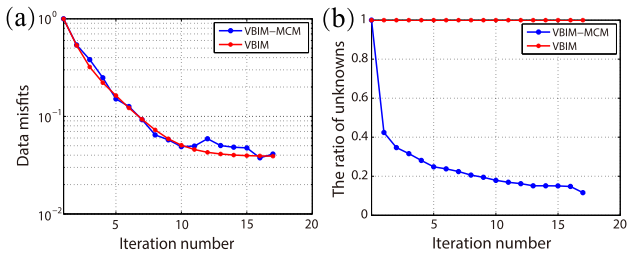

Fig. 7. Converging processes of VBIM with and without MCM. (a) Variations of data misfits of the scattered fields in different iteration steps. (b) Ratio of the number of remaining unknowns in different iteration steps to the total number of unknowns in the first step.

Fig. 6 shows the 3-D iso-surfaces of the reconstructed convex object and concave object by VBIM-MCM and VBIM. We can see that the edges and corners of the two objects are better reconstructed by VBIM-MCM. VBIM without MCM only gives the general shapes of the scatterers. Fig. 7(a) shows the variations of data misfits of the scattered fields versus iterations. The definitions of data misfit and model misfit are given in [19, eqs. (17) and (16)]. We can see that the convergence curve of VBIM is smoother than that of the VBIM-MCM. Because MCM mandatorily changes the discretized data (4) by removing redundant "background" cells, the convergence progress of VBIM interferes. As a result, local peaks and valleys show up in the convergence curve of VBIM-MCM. Fig. 7(b) shows the variations of the remaining cells in the computation domain in each iteration step. The number of unknowns decreases quickly in the first six steps for VBIM-MCM. After this, it changes slowly. Most "background" cells have been removed, and only a small number of cells will be removed in the following steps. By contrast, the cell number keeps unchanged in VBIM. Because the inversion domain is compressed by MCM, the number of unknowns is decreased. Thus, the results of VBIM-MCM are more precise.

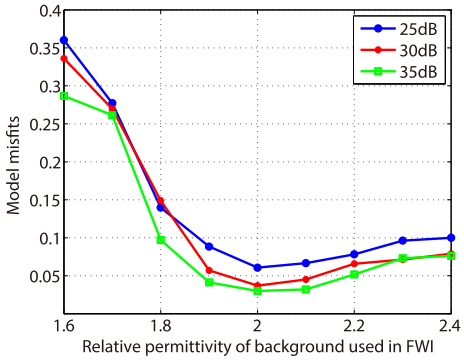

Fig. 8. Variations of model misfits versus noise levels and *a priori* information of the background relative permittivity.

Fig. 8 shows how the noise levels and *a priori* information of the background relative permittivity affect the reconstruction accuracy of VBIM-MCM. Obviously, the model misfit is the minimum when the background relative permittivity used in the FWI is the same as the true parameter 2.0. The *a priori* information of the background medium influences the reconstruction accuracy more significantly compared with the noise level.

IV. Conclusion

In this letter, we combine the FRTM imaging algorithm and the FWI algorithm VBIM to reconstruct the specific locations, shapes, and relative permittivities of subsurface objects. The FRTM first gives the approximate locations and sizes of the buried objects. Then, the FWI domain is framed inside a rectangular box enclosing the 3-D images of the subsurface objects. This manipulation greatly reduces the computation domain of the VBIM. We then perform VBIM to reconstruct the shapes and dielectric parameters of the subsurface objects enclosed inside the compressed inversion domain. Numerical results show that the MCM can further reduce the inversion domain in each VBIM iteration step. As a result, not only the shapes of the subsurface objects but also their dielectric parameters are better reconstructed by VBIM-MCM compared with VBIM without MCM.

Although this is the first attempt to combine the migration imaging and the rigorous FWI as well as the statistical method to reconstruct the model parameters of subsurface objects, the enhanced computation efficiency and improved reconstructed results show that the proposed hybrid method is reliable and feasible for subsurface imaging and detection. The future work will consider more practical engineering applications for subsurface detection. For example, when the underground moisture is taken into account, not only the loss compensation [20] must be included in the FRTM implementation but also the structural consistency is required in MCM for the reconstructed model parameters of permittivity and conductivity. In addition, when the radiation pattern of the antenna takes effect, the DGFs used in this letter are not valid since they are evaluated for infinitesimal point sources. The most straightforward method to resolve this issue is replacing the broadband GPR antenna with several point currents that can generate almost the same radiation pattern of the true antenna [21]. However, this will be left as the future work.

References

[1] H. Li, D. Song, Y. Liu, and B. Li, "Automatic pavement crack detection by multi-scale image fusion," *IEEE Trans. Intell. Transp. Syst.*, vol. 20, no. 6, pp. 2025–2036, Jun. 2019.

[2] H. Liu, X. Huang, F. Han, J. Cui, B. F. Spencer, and X. Xie, "Hybrid polarimetric GPR calibration and elongated object orientation estimation," *IEEE J. Sel. Topics Appl. Earth Observ. Remote Sens.*, vol. 12, no. 7, pp. 2080–2087, Jul. 2019.

[3] X. Feng and M. Sato, "Pre-stack migration applied to GPR for landmine detection," *Inverse Problems*, vol. 20, no. 6, pp. S99–S115, Dec. 2004.

[4] J. Zhu and L. R. Lines, "Comparison of Kirchhoff and reverse-time migration methods with applications to prestack depth imaging of complex structures," *Geophysics*, vol. 63, no. 4, pp. 1166–1176, Jul. 1998.

[5] H. Liu, Z. Long, B. Tian, F. Han, G. Fang, and Q. H. Liu, "Two-dimensional reverse-time migration applied to GPR with a 3-D-to-2-D data conversion," *IEEE J. Sel. Topics Appl. Earth Observ. Remote Sens.*, vol. 10, no. 10, pp. 4313–4320, Oct. 2017.

[6] H. Liu, B. Xing, H. Wang, J. Cui, and B. F. Spencer, "Simulation of ground penetrating radar on dispersive media by a finite element time domain algorithm," *J. Appl. Geophys.*, vol. 170, Nov. 2019, Art. no. 103821.

[7] H. Liu, Z. Long, F. Han, G. Fang, and Q. H. Liu, "Frequency-domain reverse-time migration of ground penetrating radar based on layered medium Green's functions," *IEEE J. Sel. Topics Appl. Earth Observ. Remote Sens.*, vol. 11, no. 8, pp. 2957–2965, Aug. 2018.

[8] J. Rao, M. Ratassepp, and Z. Fan, "Guided wave tomography based on full waveform inversion," *IEEE Trans. Ultrason., Ferroelectr., Freq. Control*, vol. 63, no. 5, pp. 737–745, May 2016.

[9] S. Lambot, E. C. Slob, I. Van Den Bosch, B. Stockbroeckx, and M. Vanclooster, "Modeling of ground-penetrating Radar for accurate characterization of subsurface electric properties," *IEEE Trans. Geosci. Remote Sens.*, vol. 42, no. 11, pp. 2555–2568, Nov. 2004.

[10] P. Meincke, "Linear GPR inversion for lossy soil and planar air–soil interface," *IEEE Trans. Geosci. Remote Sens.*, vol. 39, no. 12, pp. 2713–2721, Dec. 2001.

[11] A. Abubakar, P. M. Van Den Berg, and J. J. Mallorqui, "Imaging of biomedical data using a multiplicative regularized contrast source inversion method," *IEEE Trans. Microw. Theory Techn.*, vol. 50, no. 7, pp. 1761–1771, Jul. 2002.

[12] X. Chen, "Subspace-based optimization method for solving inverse-scattering problems," *IEEE Trans. Geosci. Remote Sens.*, vol. 48, no. 1, pp. 42–49, Jan. 2010.

[13] Y. M. Wang and W. C. Chew, "An iterative solution of the two-dimensional electromagnetic inverse scattering problem," *Int. J. Imag. Syst. Technol.*, vol. 1, no. 1, pp. 100–108, 1989.

[14] N. Zaiping, Y. Feng, Z. Yanwen, and Z. Yerong, "Variational Born iteration method and its applications to hybrid inversion," *IEEE Trans. Geosci. Remote Sens.*, vol. 38, no. 4, pp. 1709–1715, Jul. 2000.

[15] I. Catapano, L. Crocco, M. D. Urso, and T. Isernia, "3D microwave imaging via preliminary support reconstruction: Testing on the Fresnel 2008 database," *Inverse Problems*, vol. 25, no. 2, Feb. 2009, Art. no. 024002.

[16] M. Salucci, G. Oliveri, and A. Massa, "GPR prospecting through an inverse-scattering frequency-hopping multifocusing approach," *IEEE Trans. Geosci. Remote Sens.*, vol. 53, no. 12, pp. 6573–6592, Dec. 2015.

[17] H. Liu, Z. Deng, F. Han, Y. Xia, Q. H. Liu, and M. Sato, "Time-frequency analysis of air-coupled GPR data for identification of delamination between pavement layers," *Construct. Building Mater.*, vol. 154, pp. 1207–1215, Nov. 2017.

[18] A. Tarantola, *Inverse Problem Theory and Methods for Model Parameter Estimation*. Philadelphia, PA, USA: SIAM, 2005.

[19] T. Lan, N. Liu, F. Han, and Q. H. Liu, "Joint petrophysical and structural inversion of electromagnetic and seismic data based on vol. integral, equation method," *IEEE Trans. Geosci. Remote Sens.*, vol. 57, no. 4, pp. 2075–2086, Apr. 2019.

[20] T. Zhu, J. M. Carcione, and M. A. B. Botelho, "Reverse time imaging of ground-penetrating radar and SH-seismic data including the effects of wave loss," *Geophysics*, vol. 81, no. 4, pp. H21–H32, Jul. 2016.

[21] Y. Álvarez, F. Las-Heras, and M. R. Pino, "Reconstruction of equivalent currents distribution over arbitrary three-dimensional surfaces based on integral equation algorithms," *IEEE Trans. Antennas Propag.*, vol. 55, no. 12, pp. 3460–3468, Dec. 2007.